Additive Manufacturing Letters 14 (2025) 100312

Contents lists available at ScienceDirect

Additive Manufacturing Letters

journal homepage: www.elsevier.com/locate/addlet

Short Communication

Microstructure homogenization of laser powder bed fusion support-free low angle IN718 walls through heat treatment

Minsol Park, Mudit Kesharwani, Mohammad Attarian Shandiz, Mathieu Brochu *

Department of Mining and Materials Engineering, McGill University, Montreal, QC H3A 0C5, Canada

ARTICLE INFO

Keywords:
Laser powder bed fusion
Inconel 718
support-free low angle overhangs
precipitation hardening

ABSTRACT

This study investigates the effectiveness of heat treatment (HT) to homogenize the microstructural and mechanical asymmetry between the bulk and the downskin regions of support-free IN718 walls fabricated at angles of 30°, 20°, 15°, and 10° In the as-built condition, the microhardness ranged from 340 ± 5 HV to 351 ± 4 HV for the bulk and from 315 ± 4 HV to 323 ± 10 HV for the downskin region, resulting in a maximum difference range of 35 HV. The HT eliminated this difference where microhardness values of 482 ± 3 HV in the bulk and 478 ± 4 HV in the downskin were measured. The HT induced γ'' precipitation with volume fraction and mean precipitate size in the bulk of 16.6 % and 24.7 ± 7.3 nm. These values are statistically comparable to those in the downskin: 15.8 % and 26.5 ± 7.9 nm. The similarity in the γ'' characteristics explains the recovery of the mismatch in hardness as γ'' contributes approximately 85 % of the strengthening in the HT condition.

1. Introduction

Laser Powder Bed Fusion (LPBF) uses a laser as the primary energy source to selectively melt metal powders, creating a meltpool that solidifies into discrete tracks, layers, and eventually into complex three-dimensional structures [1]. Over the past decade, advancements in LPBF have prompted a sustained demand for support-free, low-overhang geometries [2]. This demand is driven by the significant benefits of minimized labor requirements for post-processing and support structure removal, leading to reduced manufacturing costs and time by up to 29 % [3]. Recent studies highlight the feasibility of fabricating support-free low-overhang features with angles below 30 degrees and even as low as 0° [4–8]. However, due to differences in cooling rates between the bulk material and the downskin (DS) region, distinct microstructures develop. Kumar at al., [9] reported for unsupported IN625 walls, the bulk region exhibited a cellular structure with a primary dendrite arm spacing (PDAS) of 0.7 ± 0.2 μm, corresponding to a cooling rate of 2.3×10^5 K/s, while the DS region showed a coarser dendritic microstructure with a PDAS of 4.7 ± 2.1 μm, reflecting a lower cooling rate of 8.2×10^3 K/s. This disparity leads to a mismatch in microhardness, measured at 322 ± 17 HV for the bulk and 278 ± 18 HV for the DS [9]. Kumar et al. [9] reported that heat treatment (HT) at 1150 °C inverted this microhardness mismatch. Under a HT condition, the microhardness measured were 252 ± 15 HV for the bulk and 271 ± 10 HV for the DS. This effect is attributed to variations in recrystallization and grain growth between the bulk and DS regions. They also noted that HT at temperatures below 1150 °C can lead to the nucleation of the detrimental delta (δ) phase.

The current study investigates if HT would be effective to eliminate the bulk/downskin microstructure mismatch in IN718, a precipitation hardened alloy. IN718 support-free walls with overhang angles of 30°, 20°,15°, and 10° were fabricated using LPBF process. These samples were subjected to a solution treatment and double aging HT. Microhardness measurements were conducted on four regions of interest (ROIs): AB-Bulk, AB-DS, HT-Bulk, and HT-DS, to assess and compare their mechanical performance. A theoretical flow stress approach was used to clarify the contributions of various strengthening mechanisms known for IN718. The respective strengthening contributions were documented by microstructural analyses using Scanning Electron Microscopy (SEM) in conjunction with Electron Backscatter Diffraction (EBSD), Energy Dispersive Spectroscopy (EDS), and image analysis.

2. Experimental methodologies

IN718 powder sourced from Carpenter with the chemical composition detailed in Table 1, was utilized to fabricate a series of support-free walls. The dimensions of the walls were maintained constant with an overhang length of 60 mm, a width of 10 mm, and a thickness of 7 mm, while the overhang angle (θ) was varied at 30°, 20°,15°, and 10° The

---

* Corresponding author.
E-mail address: mathieu.brochu@mcgill.ca (M. Brochu).

https://doi.org/10.1016/j.addlet.2025.100312
Received 7 April 2025; Received in revised form 6 July 2025; Accepted 24 July 2025

fabrication was performed using the Renishaw AM500E LPBF system equipped with a 500 W Nd: YAG laser fiber laser. The process parameters optimization methodology that is based on bulk sections parameters (power: 200 W, exposure time: 70 μs, point distance: 70 μm, hatch distance: 90 μm, and layer thickness: 30 μm) can be found in [10].

The HT was performed using a Carbolite STF 15–450 tube furnace in accordance with the AMS 5664 standard [12]. The homogenization treatment of the AB samples was conducted at 1065 °C for 1 hour, followed by air cooling to a room temperature. The samples were maintained at 750 °C for 10 h as the first aging stage, followed by furnace cooling to 620 °C. The final aging stage was performed at 650 °C for a duration of 8 h, after which the samples were air-cooled to ambient temperature. The cross-sections of both AB and HT samples were prepared by grinding up to 800 grit using SiC abrasive paper. Subsequent polishing was performed using cloths with diamond suspensions of 9 μm, 3 μm, and 1 μm, respectively. Electrolytic etching was performed on the polished sample using a solution of 12 ml H_3PO_4, 40 ml HNO_3, and 48 ml H_2SO_4 at 5 V for approximately 5 s. The optical micrographs of the etched samples were obtained using an optical Keyence VHX-5000 digital light microscope. Downskin thicknesses were quantified by conducting 100 individual measurements from 5 different micrographs using ImageJ software. Vickers microhardness measurements were performed using a Clark CM-100AT microhardness indenter with a 200 gf load, repeated 15 times for each ROIs. Microhardness was also measured at incremental distances of 250 μm from the downskin region to evaluate changes in hardness as a function of distance from the DS. Reported values represent averages, and error bars indicate the standard deviation of the measurements. To investigate the grain morphology, EBSD mapping was conducted over an area of 1.0 mm x 1.5 mm, extending from the bottom edge of the sample to encompass both bulk and DS regions. Grain size was determined based on the equivalent circle diameter of high-angle grain boundaries (misorientation >15°) using HKL Channel 5 software. Kernel Average Misorientation (KAM) maps were also generated using the HKL Channel 5 software. The geometrically necessary dislocation (GND) density, ρ_{GND}, was calculated from the KAM data using the relation $\rho_{GND} = \frac{\theta}{bl}$, where θ is the local misorientation angle, b is the Burgers vector, valued at 0.25 nm for IN718 [13], and l is the step size of 0.9 μm. EDS mappings were acquired using a SEM Hitachi SU3500 to determine the elemental distribution of Ni, Nb, Mo, Cr, C, Ti, Al, and Fe. SEM micrographs of the precipitates (γ' and γ'') in the HT-Bulk and HT-DS were captured using a SEM Hitachi SU8000. ImageJ software was employed to measure the PDAS of the AB samples and to quantify the size of γ' and γ'' from the SEM micrographs. X-ray Diffraction (XRD) analysis was conducted using a Bruker D8 DISCOVER system with CuKα₁ radiation (wavelength of 0.154056 nm) to determine the volume fractions of γ, γ', and γ'' phases through peak fitting [14–16]. Analysis of Variance (ANOVA) tests were conducted to evaluate differences within the data sets. In this study, a p-value threshold was set whereby values greater than 0.01 were considered to indicate no significant difference. Profilometry-based indentation plastometry (PIP) [17,18] was performed to acquire the stress–strain curves for the four regions of interest using the PLX-Benchtop system. The analysis used a 0.5 mm diameter indenter tip. The indentation was conducted in the normal direction to the surface for the four regions. Prior to testing, the surfaces were prepared to a minimum finish of 1200 grit paper using standard metallographic procedures.

3. Results and discussion

3.1. DS thickness analysis of AB and HT samples

Fig. 1 (a-d) presents the etched optical micrographs of the AB samples, revealing the two distinct regions, bulk and DS. As depicted in Fig. 1, the DS thickness increases from 128±32 μm to 297±55 μm as the overhang angle decreases from 30° to 10° This increase in thickness is geometrically-driven and corresponds to the increase in overhang length and DS area, as described by eq.1 [19] :

$$S = H \times cot(\theta) \tag{1}$$

where H represents the layer thickness, and θ is defined as the angle between the horizontal plane and the tangent line of a given surface.

Following HT, the distinction between the bulk and DS regions is no longer evident in the optical micrographs, as illustrated in Fig. 1 (e-h). This observation suggests a potential homogenization of the microstructure. To delineate the boundary between these regions, the DS thickness of the AB samples was used as a point of reference.

3.2. Vickers microhardness analysis of AB and HT samples

Table 2 summarizes the Vickers microhardness measurements for the sample at a 10–30° overhang. AB-Bulk values ranged from 340 ± 5 HV to 351 ± 4 HV, which are in close agreement with the literature-reported value of 339 HV [11]. On the other hand, the AB-DS ranged from 315 ± 4 HV to 323 ± 10 HV, yielding a distinct hardness difference of 25–35 HV between the bulk and the DS regions. After heat treatment, microhardness values ranged from 482 ± 3 HV to 484 ± 6 HV for bulk and 478 ± 4 HV to 481 ± 4 HV for DS, aligning with the AMS 5664 standard for HT-IN718 (459–511 HV) [20]. ANOVA analysis ($p > 0.03$ for all angles) indicates no statistically significant difference between bulk and DS regions for all angles, confirming effective homogenization of microhardness and suggesting concurrent microstructural uniformity in the precipitation-hardened IN718 alloy within the 10–30° range. For clarity and focus, only the 15° overhang data—where the AB condition exhibited the maximum microhardness difference of 35 HV—is discussed in detail in this work.

IN718, a precipitation-hardened alloy, demonstrates uniform microhardness across both bulk and DS regions after HT as shown in Fig. 2a. In contrast, IN625, a solid solution-strengthened alloy, exhibits the typical response where microhardness homogenization is not achievable through HT. As reported by Kumar et al. [9], IN625 shows a decreasing microhardness gradient in the as-built condition—from 322 ± 17 HV in the bulk to 278 ± 18 HV in the DS, as shown in Fig. 2b The solution treatment reverses this gradient, increasing microhardness from 252 ± 15 HV (bulk) to 271 ± 10 HV (DS). This contrast highlights the significance of the present work, where precipitation hardening in IN718 enables effective mechanical property homogenization in support-free low overhang structures.

3.3. Strengthening mechanisms of AB and HT samples

Microhardness is influenced by various strengthening mechanisms, including friction stresses, Hall-Petch strengthening, and precipitation strengthening [21]. While empirical relationships can approximate these hardening contributions, the theoretical flow stress (σ_{flow}) approach to understand the current results was taken as it provides a more accurate measure of the combined strengthening effects [22]. The

Table 1
The starting IN718 powder feedstock chemical composition as per the certificate of conformity of the supplier [11].

Element	Ni	Nb	Mo	Cr	C	Ti	Al	Fe	Si	Mn
Wt. (%)	52.37	5.25	3.07	19.19	0.04	0.93	0.64	18.22	0.15	0.14

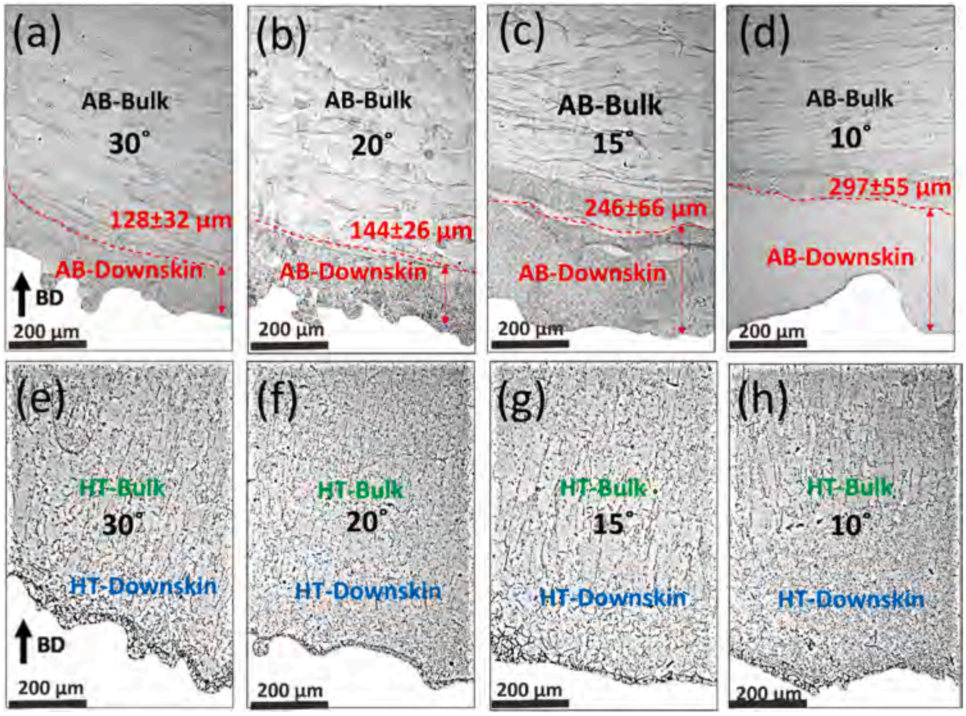

Fig. 1. Etched optical micrograph of AB-IN 718 at angles of (a) 30° (b) 20° (c) 15° (d) 10° showing the variation of downskin thickness with the printing angle and of HT-IN 718 at angles of (e) 30° (f) 20° (g) 15° (h) 10° showing the microstructural homogenization between the bulk and the DS.

Table 2
Microhardness of the IN718 at an angle of 10–30° across different ROIs.

	As-built				Heat-treated			
ROI	10°	15°	20°	30°	10°	15°	20°	30°
Bulk	340 ± 5	350 ± 10	351 ± 4	351 ± 4	483 ± 4	482 ± 3	483 ± 5	484 ± 6
DS	315 ± 4	315 ± 5	317 ± 6	323 ±10	480 ± 5	478 ± 4	480 ± 2	481 ± 4
Difference	25	35	34	28	3	4	3	3

flow stress equation is defined as follow:

$$\sigma_{\text{flow}} = \sigma_o + \Delta\sigma_{ss} + \Delta\sigma_{HP} + \Delta\sigma_d + \Delta\sigma_{\text{pre}} \quad (2)$$

Where σ_o refers to internal stress, $\Delta\sigma_{SS}$ corresponds to solid-solution strengthening, $\Delta\sigma_{HP}$ signifies Hall-Petch strengthening, $\Delta\sigma_d$ stands for dislocation strengthening and $\Delta\sigma_{pre}$ represent precipitation strengthening.

3.3.1. *Internal stress*

The internal stress can be defined as [16]:

$$\sigma_0 = M\tau_{crss} \quad (3)$$

where M represents the Taylor factor, valued at 3.06 for Ni-based superalloys [23], and τ_{crss} denotes the critical resolved shear stress, which is 17.5 MPa for Ni-based superalloys [24]. An internal stress of 48 MPa is derived and assumed to remain consistent across all ROIs in this study.

3.3.2. *Solid-solution strengthening*

The solid-solution strengthening component can be quantified by [25]:

$$\Delta\sigma_{ss} = \left(\sum_i k_i^2 C_i\right)^{1/2} \quad (4)$$

where k_i denotes the strengthening constant for solute atom i, C_i is the concentration of solute atom i. The C_i and k_i values for IN718 are given in Table 1 and 3 respectively. For AB-bulk and AB-DS, the solid-solution strengthening is calculated to be 319 MPa using the provided C_i and k_i

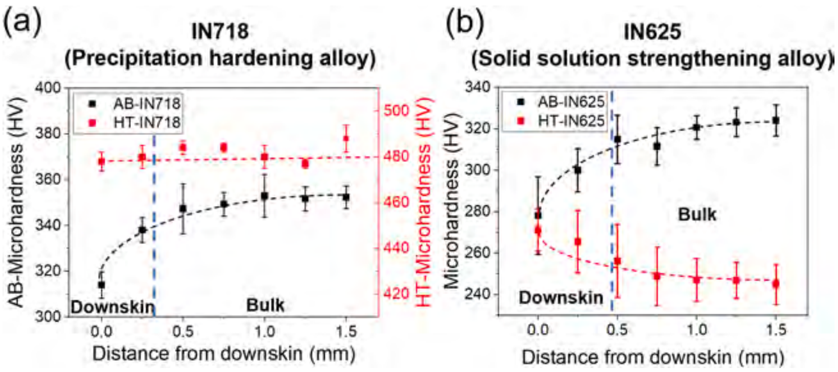

Fig. 2. Plots the average microhardness against the distance from downskin for (a) AB and HT IN718 and (b) AB and HT IN625 [9].

values. On the other hand, some alloying elements concentrations will vary through precipitation during HT [16]. Consequently, for both HT-Bulk and HT-DS, a solid-solution strengthening value of 255 MPa is assumed, based on the chemical analysis of the matrix of a homogenized and double-aged (HDA) IN718 [16].

3.3.3. Hall-Petch strengthening

Fig. 3a and 3b show the EBSD mapping of AB and HT samples with pole figures {100}, {110} and {111} orientations. The grain size and aspect ratio (AR) data are summarized in Table 4. In the AB bulk region, a pronounced texture with a maximum Multiple of Uniform Density (MUD) of 5.03 in the build direction (X) is evident in the {100} pole figure (Fig. 3a). Elongated grains with an average grain size of 31.1 ± 10.9 μm and an AR of 3.7 ± 2.0 were measured. This grain morphology is characteristic of LPBF metals, where the processing parameters, thermal gradient and solidification front velocity combination promotes strong texture and epitaxial grains in the build direction [27]. The AB-DS region exhibits a lower intensity texture (MUD of 3.32) with a finer grain size of 15.8 ± 13.5 μm, and a reduced AR of 1.9 ± 0.6. results from the differences in the thermal gradient (G) and growth rate (R) experienced by the DS region during solidification, which is driven by heat accumulation from the powder bed [4]. After HT, differences in grain structure between the bulk and DS regions were revealed through EBSD, though no such distinction was observable in optical micrographs. In HT-Bulk, recrystallization and grain growth were evident, producing a lower intensity texture (MUD of 2.95) with an increased grain size of 44.3 ± 27.8 μm and a reduced AR of 2.3 ± 1.4. In contrast, the HT-DS region showed no significant morphological changes post-HT, retaining a grain size of 16.0 ± 11.6 μm and an AR of 1.9 ± 0.7. The ANOVA test confirmed that the grain size and AR of the AB-DS and HT-DS were statistically similar, with p values of 0.68 and 0.76 respectively. This lack of grain evolution in the HT-DS region is explained by insufficient stored strain energy to drive recrystallization and grain growth, as previously reported by Kumar et al. [9]. The ρ_{GND} within a grain serves as a key parameter for correlating the stored strain energy with the grain's recrystallization behavior [28]. Figs. 3c and 3d present the KAM map and the corresponding ρ_{GND} histogram, respectively. The median ρ_{GND} values were 2.4×10^{14} m^{-2} for AB-Bulk, 1.0×10^{14} m^{-2} for AB-DS, 0.4×10^{14} m^{-2} for HT-Bulk, and 0.9×10^{14} m^{-2} for HT-DS, as summarized in Table 4. A significant drop in median ρ_{GND} approximately 2×10^{14} m^{-2}—was observed in the bulk region post-heat treatment, whereas the ρ_{GND} in the downskin region remained unchanged. This further supports the conclusion that the downskin region lacks sufficient stored strain energy to drive recrystallization and grain growth. The detailed mechanisms of strain energy storage and recrystallization behavior in the downskin region have been comprehensively discussed by Kumar et al. [9].

Fig. 4 presents SEM micrographs with EDS mapping of the various ROIs. As illustrated in Fig. 4a, in AB-Bulk, a columnar dendritic structure with a PDAS of 0.5 ± 0.1 μm is observed. In contrast, Fig. 4b displays coarser dendritic microstructures in the AB-DS region, with a PDAS of 1.2 ± 0.3 μm. These microstructural characteristics and PDAS values align with the reported findings for IN625, which shows a PDAS of 0.7 ± 0.2 μm in AB-Bulk and 1.3 ± 1.1 μm in AB-DS [29]. The coarser dendritic microstructures in the AB-DS region can be attributed to the reduced solidification rate, which results from localized heat accumulation due to the low thermal conductivity and limited heat extraction capability of the powder bed [2]. EDS mapping of both AB-Bulk and AB-DS regions revealed evidence of microsegregation of Nb and Mo within the interdendritic regions. Given the lower partition coefficients of Mo (0.766) and Nb (0.271) [30], these elements preferentially segregate into the interdendritic spaces during solidification [31].

Table 3
IN718 strengthening constant (k_i) [26].

Element	Nb	Mo	Cr	Ti	Al	Fe
k_i	1183	1015	337	775	225	153

Compared to the AB condition, the homogenized microstructures in both the HT-Bulk and HT-DS regions show evident dissolution of cellular structures, as shown in Figs. 4c and 4d In these regions, MC-type carbides enriched with Nb, Mo, and C are primarily located at grain boundaries, accompanied by local depletion of Ni, Fe, and Cr [11].

The Hall-Petch relationship, which describes the inverse correlation between a characteristic microstructural length scale and material strength, is expressed as: [32]:

$$\Delta\sigma = k_y d^{0.5} \tag{5}$$

where k_y denotes the Hall-Petch coefficient with a value of 158 MPa μm for Ni-superalloy [23] and d is the characteristic length scale of the microstructure, either cell or grain size. Although traditionally applied to grain size, the Hall-Petch relationship can also be extended to other microstructural barriers to dislocation motion, such as sub-grain structures or solidification cells, provided they serve as effective obstacles to plastic deformation [4,16].

In AB conditions, the microstructure is dominated by columnar dendrites, and the PDAS serves as the effective length scale for strengthening rather than the grain size. Using the PDAS values of 0.5 ± 0.1 μm and 1.2 ± 0.3 μm for the AB-Bulk and AB-DS regions, respectively, the Hall-Petch strengthening contributions are estimated to be 223 MPa and 145 MPa. These results reflect the finer dendritic structure present in the bulk relative to the downskin region.

Following HT conditions, the dendritic microstructure is no longer preserved, and grain boundaries become the dominant strengthening mechanism. As such, the grain size replaces PDAS in the Hall-Petch equation. The recrystallized grains in HT-Bulk, with an average size of 44.3 ± 27.8 μm, contributed 24 MPa to the Hall-Petch strengthening. In contrast, HT-DS underwent homogenization without recrystallization or substantial grain growth, resulting in grains of 16.0 ± 11.6 μm and a 16 MPa contribution. The substantial reduction in strengthening after heat treatment is attributed to grain coarsening and the elimination of fine dendritic features.

3.3.4. Dislocation strengthening

The dislocation strengthening was quantified using equation 6 [16]:

$$\Delta\sigma_d = BMbG\rho_{GND}{}^{0.5} \tag{6}$$

where B is a coefficient of proportionality valued at 0.2 [16], G is the shear modulus, valued at 76 GPa for IN718 [13]. The dislocation strengthening contribution was calculated to be 183 MPa for AB-Bulk and 120 MPa for AB-DS, corresponding to dislocation densities of 2.4×10^{14} m^{-2} and 1.0×10^{14} m^{-2}, respectively. After HT, the dislocation strengthening contribution decreased to 74 MPa for HT-Bulk and 113 MPa for HT-DS, with corresponding dislocation densities of 0.4×10^{14} m^{-2} and 0.9×10^{14} m^{-2}, respectively.

3.3.5. Precipitation strengthening

In order to calculate the precipitation strengthening contribution, an analysis of the microstructure was performed. Due to the high cooling rates characteristic of LPBF, ranging from 0.05 to 3×10^6 K/s [33], the formation of γ' and γ'' precipitates is significantly restricted. The cooling rate required for γ'' precipitate formation is below 100 K/s, explaining their absence in the AB condition [34]. Consequently, the precipitation strengthening contribution is neglected from the analysis due to the absence of precipitates in the AB conditions.

The solution treatment at 1065 °C eliminated the microsegregation and produced a uniform chemical distribution within the austenitic γ matrix. During the first aging stage at 750 °C, the γ matrix partially transforms into γ'' (Ni_3Nb) through the reaction $\gamma \rightarrow \gamma + \gamma''$. In the second aging stage at 650 °C, further precipitation of both γ' ($Ni_3(Al, Ti)$) and γ''

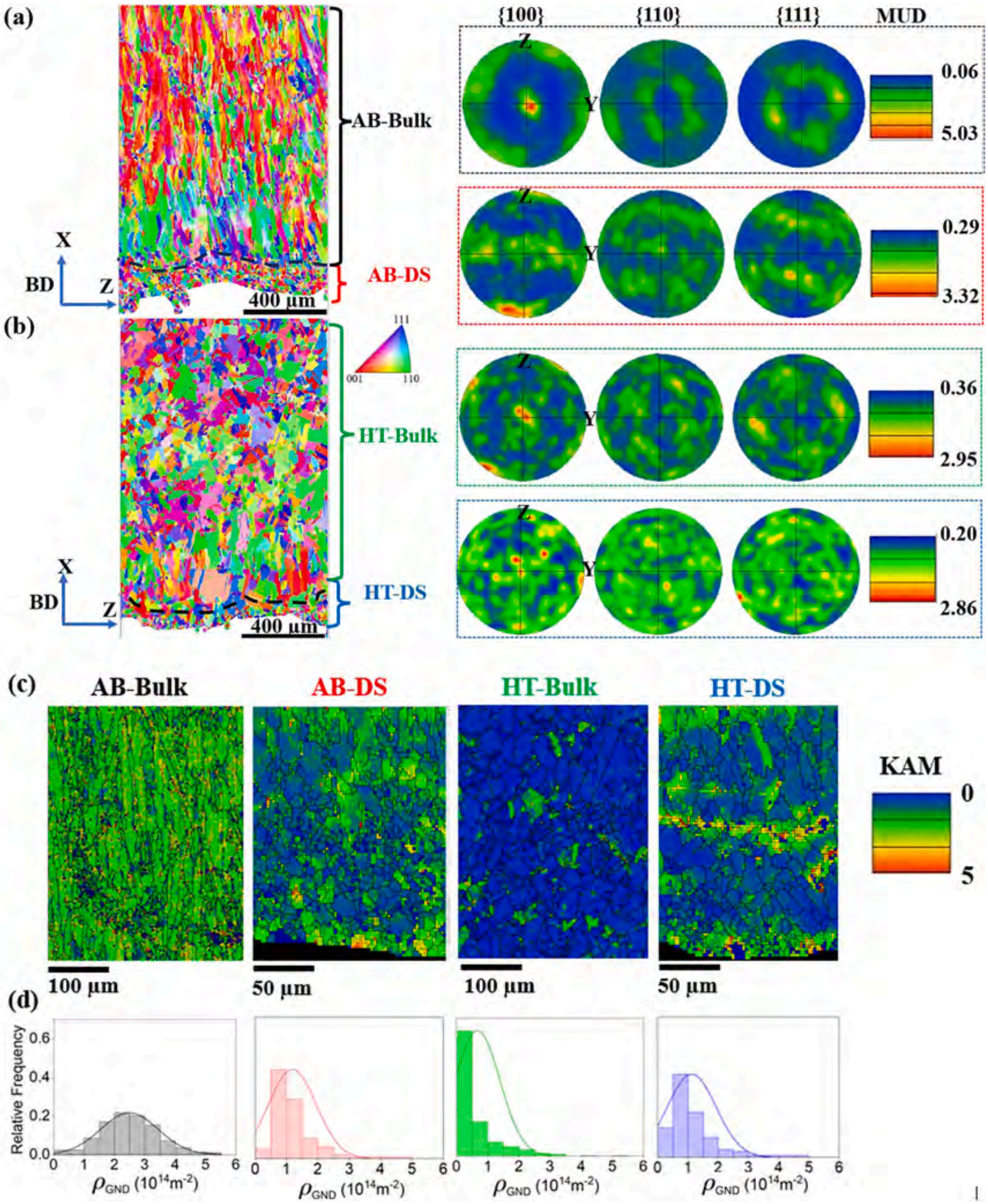

Fig. 3. EBSD mapping of (a) AB and (b) HT overhangs at an angle of 15°, with {100}, {110} and {111} pole figures, (c) KAMs map and (d) GND histogram.

Table 4
EBSD parameters of the IN718 at an angle of 15° across different ROIs.

ROI	Grain size (μm)	Aspect ratio	Median ρ_{GND} (× $10^{14}m^{-2}$)
AB-Bulk	31.8 ± 11.7	3.1 ± 2.3	2.4
AB-DS	15.8 ± 13.5	1.9 ± 0.6	1.0
HT-Bulk	44.3 ± 27.8	2.3 ± 1.4	0.4
HT-DS	16.0 ± 11.6	1.9 ± 0.7	0.9

phases occurs, following the reaction $\gamma + \gamma'' \rightarrow \gamma + \gamma' + \gamma''$. Fig. 5 presents high-resolution SEM micrographs of the HT-Bulk and HT-DS regions. The micrographs are showing comparable precipitation of both γ' and γ'' phases. Here, γ' appears as small spherical particles, while γ'' has a disklike morphology oriented along [100] and [111] directions [35]. The mean diameters of γ' and γ'' in the HT-Bulk were 11.8 ± 2.5 nm and 24.7 ± 7.4 nm, respectively. The mean diameters in the HT-DS were 12.1 ± 2.0 nm for γ' and 26.5 ± 8.0 nm for γ''. ANOVA testing comparing the respective sizes yielded $p = 0.74$ for γ' and $p = 0.21$ for γ'', indicating that the precipitate characteristics are statistically identical between the HT-Bulk and HT-DS regions. The obtained values are consistent with literature data for HDA - IN718, showing γ' precipitate sizes of 5–50 nm [36] and γ'' sizes of 14–38 nm [16]. The aspect ratio of γ'' ($AR_{\gamma''}$) is found to be 3.2 for both HT-Bulk and HT-DS, which falls within the reported literature range of 2.3 to 3.7 for HDA-IN718 [37].

Fig. 6 presents the XRD analysis, where peak deconvolution was conducted to isolate the peaks for γ, γ', and γ'' phases through curve fitting [14–16]. As presented in Table 5, the volume fractions of γ' and γ'' in the HT-Bulk were 6.6 ± 1.2 % and 16.6 ± 1.4 %, respectively. The same volume fractions in HT-DS were 5.6 ± 0.9 % and 15.8 ± 1.2 %.

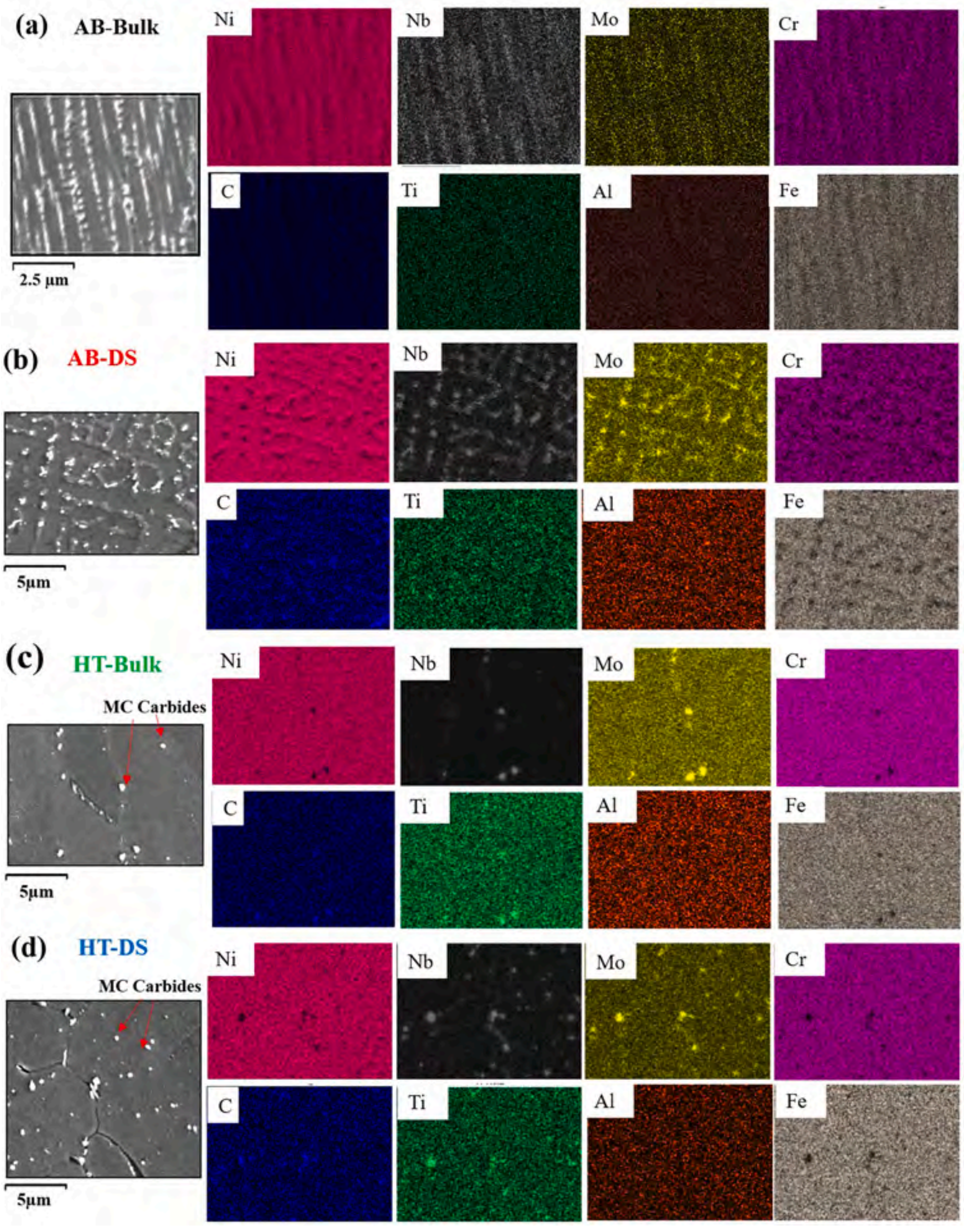

Fig. 4. SEM micrographs of IN718 printed at an angle of 15° and EDS mapping with the elemental maps of Ni, Nb, Mo, Cr, C, Ti, Al, and Fe for (a) AB-Bulk, (b) AB-DS, (c) HT-Bulk and (d) HT-DS.

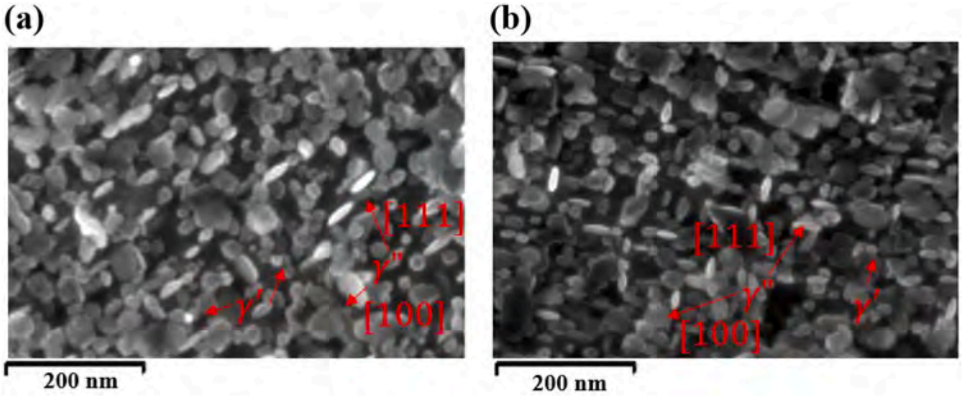

Fig. 5. SEM micrographs showing the γ'' and γ' precipitates for (a) HT-Bulk and (b) HT-DS.

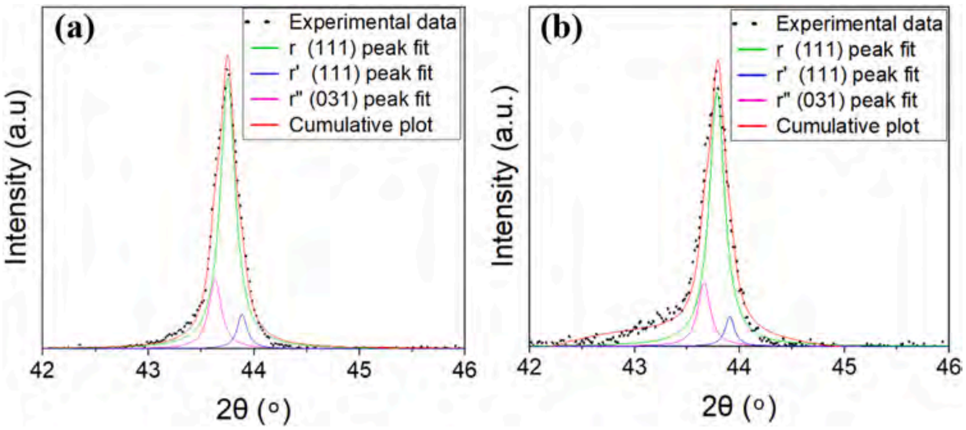

Fig. 6. Peak deconvolution of XRD signal into peak fits of γ, γ' and, γ'' with the cumulative plot for (a) HT-Bulk and (b) HT-DS.

Table 5
Precipitates parameters for the IN718 at an angle of 15° across HT-ROIs.

ROI	γ' mean diameter (nm)	γ'' mean diameter (nm)	γ' volume fraction (%)	γ'' volume fraction (%)
HT-Bulk	11.8 ± 2.5	24.7 ± 7.4	6.6	16.6
HT-DS	12.1 ± 2.0	26.5 ± 8.0	5.6	15.8

The ANOVA test results indicated that these values for HT-Bulk and HT-DS are statistically similar, with $p = 0.09$ for γ' and $p = 0.49$ for γ''. Moreover, these values are consistent with literature findings, which report γ' and γ'' volume fractions of 5.1 % and 15.5 %, respectively for HDA-IN718 [16].

In the current samples, coherency strengthening from the γ' and γ'' phases is a dominant effect rather than the order strengthening [16], while the Orowan strengthening mechanism is not operative. The experimental data indicate that the maximum diameters of the precipitates are 16.4 nm for γ' and 41.3 nm for γ''. These values are both below the threshold diameters required for coherency-to-Orowan strengthening transitions, which are 34 nm and 46 nm, respectively [16]. The precipitation strengthening was determined by summing the contributions of coherency strengthening from the γ' and γ'' phases as expressed [13,16,38]:

$$\Delta\sigma_{pre} = 3MG\delta_{\gamma'}^{3/2}\left[\frac{D_{\gamma'}f_{\gamma'}}{2b}\right]^{0.5} + 1.7MG\delta_{\gamma''}^{3/2}\left[\frac{D_{\gamma''}f_{\gamma''}(1-\beta)}{2bAR_{\gamma''}^{2}}\right]^{0.5} \tag{7}$$

where lattice misfits for the γ' and γ'' phases are denoted by $\delta_{\gamma'}$ *and* $\delta_{\gamma''}$, valued at 0.001 % and 0.023 % respectively [16] and $D_{\gamma'}$ and $D_{\gamma''}$ refer to the mean diameter for the γ' and γ'' phases. The volume fractions of these phases are indicated by $f_{\gamma'}$ and $f_{\gamma''}$, with β set to 1/3 to account for the presence of precipitates distributed equally among the three variants [13]. The precipitation strengthening contribution HT-Bulk and HT-DS was calculated at 771 MPa and 715 MPa, respectively.

3.3.6. *Flow stress*

Table 6 summarizes the contributions of the distinct strengthening mechanisms to the flow stress ROIs studied in this work. The calculated contributions were 773 MPa for AB-Bulk and 632 MPa for AB-DS. While the AB-Bulk prediction closely aligned with the literature-reported value of 790 MPa, the AB-DS calculation exhibited a significant deviation [11]. The observed difference between the bulk and downskin regions is consistent with the corresponding hardness values reported in Table 2, Section 3.2, where the AB-Bulk exhibits a hardness of 350 ± 10 HV compared to 315 ± 5 HV for the AB-DS.

On the other hand, HT-Bulk and HT-DS have calculated flow stresses of 1172 MPa and 1147 MPa, respectively, closely aligning with the literature-reported benchmark of 1189 MPa [16]. This consistency is further reflected in the comparable microhardness values of 482 ± 3 HV and 478 ± 4 HV, with an ANOVA test yielding a p-value of 0.03, as shown in Table 2. The minimal difference in microhardness between these regions is primarily attributed to the dominant contribution of precipitation strengthening in IN718, which accounts for over 85 % of the total flow stress in the HT condition. This mechanism effectively mitigates the influence of microstructural gradients.

To validate the modeled flow stress values presented in Table 6, PIP testing was performed due to the sub-millimeter thickness of the downskin region. The nominal PIP stress–strain curves are shown in Fig. 7. The measured yield strength for the four ROIs, reported in Table 6, are 734 MPa (AB-Bulk), 666 MPa (AB-DS), 1273 MPa (HT-Bulk), and 1223 MPa (HT-DS), respectively. These values are matching with the modeled flow stresses of 773, 632, 1172, and 1147 MPa, respectively. The comparison of the data showed deviation of 5, 5, 6 and 8 %, respectively

This work demonstrates that for precipitation hardening alloys, such as IN718, the HT can effectively resolve discrepancies in microstructure and microhardness between the bulk and DS regions that are found in support-free low angle overhang. This is the opposite case than for solid-solution strengthened alloys, such as IN625, where the microstructure mismatch cannot be addressed by HT [9].

4. Conclusion

This study demonstrated the possibility to homogenize the microstructure and mechanical properties of IN718 between bulk and DS in support-free overhang using post-process HT. The initial microhardness difference between the bulk (350 ± 10 HV) and the DS (315 ± 5 HV) regions in the AB condition was eliminated following HT, where microhardness of the HT-Bulk and HT-DS were values of 482 ± 3 HV and 478 ± 4 HV, respectively. Post-HT, both HT-Bulk and HT-DS regions exhibited comparable microstructural features, including MC carbides localized at grain boundaries and the precipitation of γ' and γ'' phases. The mean diameter of γ'' in HT-Bulk (24.7 ± 7.3 nm) were statistically similar to that in HT-DS (26.5 ± 7.9 nm). The volume fractions of the γ'' in HT-Bulk and HT-DS were 16.6 ± 1.4 % and 15.8 ± 1.2 %, respectively. The precipitation strengthening contribution was 771 MPa in HT-Bulk and 715 MPa in HT-DS which contributed to 85 % of the calculated flow stress variation.

Table 6
Flow stress components of the IN718 at 15° in different ROIs.

ROI	Internal stress (σ_0) (MPa)	Solid Solution strengthening ($\Delta\sigma_{SS}$) (MPa)	Hall-Petch strengthening		Dislocation strengthening ($\Delta\sigma_d$) (MPa)	Precipitation strengthening ($\Delta\sigma_{pre}$) (MPa)	Modeled flow stress (σ_{flow}) (MPa)	Measured yield strength (MPa)
			Cell boundaries ($\Delta\sigma_c$) (MPa)	Grain boundaries ($\Delta\sigma_c$) (MPa)				
AB-Bulk	48	319	223	–	183	–	773	734
AB-DS	48	319	145	–	120	–	632	666
HT-Bulk	48	255	–	24	74	771	1172	1273
HT-DS	48	255	–	16	113	715	1147	1223

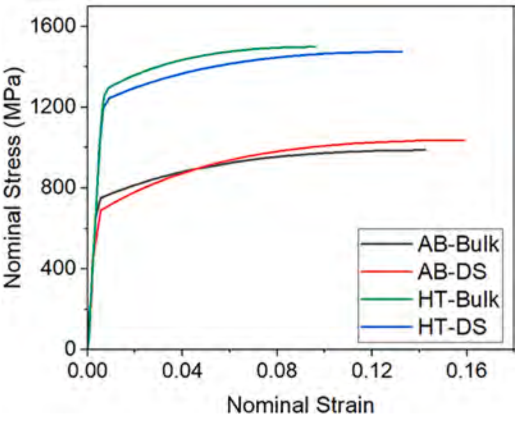

Fig. 7. Nominal stress-strain plots of the overhang 10-degree sample obtained from PIP.

Declaration of generative AI and AI-assisted technologies in the writing process

Statement: During the preparation of this work the author(s) used Chat GPT 4.0 in order to improve the readability and language of the manuscript, without generating content. After using this tool/service, the author(s) reviewed and edited the content as needed and take(s) full responsibility for the content of the published article.

CRediT authorship contribution statement

Minsol Park: Writing – original draft, Visualization, Validation, Software, Resources, Methodology, Investigation, Formal analysis, Data curation, Conceptualization. **Mudit Kesharwani:** Visualization, Validation, Investigation, Formal analysis, Data curation. **Mohammad Attarian Shandiz:** Software, Methodology. **Mathieu Brochu:** Writing – review & editing, Supervision, Resources, Project administration, Funding acquisition, Conceptualization.

Declaration of competing interest

The authors declare that they have no known competing financial interests or personal relationships that could have appeared to influence the work reported in this paper.

Acknowledgements

The authors would like to acknowledge Natural Sciences and Engineering Research Council of Canada (NSERC CRDPJ 517633–17) for their support.

Data availability

Data will be made available on request.

References

[1] S. Chowdhury, N. Yadaiah, C. Prakash, S. Ramakrishna, S. Dixit, L.R. Gupta, D. Buddhi, Laser powder bed fusion: a state-of-the-art review of the technology, materials, properties & defects, and numerical modelling, J. Mater. Res. Technol. 20 (2022) 2109–2172, https://doi.org/10.1016/j.jmrt.2022.07.121.

[2] V. Viale, J. Stavridis, A. Salmi, F. Bondioli, A. Saboori, Optimisation of downskin parameters to produce metallic parts via laser powder bed fusion process: an overview, Int. J. Adv. Manuf. Technol. 123 (2022) 2159–2182, https://doi.org/10.1007/s00170-022-10314-z.

[3] J. Jiang, X. Xu, J. Stringer, Support structures for additive manufacturing: a review, J. Manuf. Mater. Process. 2 (2018), https://doi.org/10.3390/jmmp2040064.

[4] A. Kumar, M.A. Shandiz, F. Sikan, M. Brochu, Microstructural and mechanical properties of an internal support-free IN625 closed impeller manufactured via laser

powder bed fusion (L-PBF), Mater. Sci. Eng. A 874 (2023) 145080, https://doi.org/10.1016/j.msea.2023.145080.

[5] Q. Han, H. Gu, S. Soe, R. Setchi, F. Lacan, J. Hill, Manufacturability of AlSi10Mg overhang structures fabricated by laser powder bed fusion, Mater. Des. 160 (2018) 1080–1095, https://doi.org/10.1016/j.matdes.2018.10.043.

[6] F. Calignano, Design optimization of supports for overhanging structures in aluminum and titanium alloys by selective laser melting, Mater. Des. 64 (2014) 203–213, https://doi.org/10.1016/j.matdes.2014.07.043.

[7] J.D. Roehling, W.L. Smith, T.T. Roehling, B. Vrancken, G.M. Guss, J.T. McKeown, M.R. Hill, M.J. Matthews, Reducing residual stress by selective large-area diode surface heating during laser powder bed fusion additive manufacturing, Addit. Manuf. 28 (2019) 228–235, https://doi.org/10.1016/j.addma.2019.05.009.

[8] C.K. Sit, L.N.S. Chiu, Y. Tang, A. Huang, Towards supportless laser powder bed fusion: fundamental understanding of the formation of 1st layer overhang through parameter optimisation and in-situ high-speed thermal imaging, Virtual Phys. Prototyp. 18 (2023), https://doi.org/10.1080/17452759.2023.2231906.

[9] A. Kumar, M.A. Shandiz, M. Brochu, Solution heat treatment of support-free IN625 overhang sections fabricated via laser powder bed fusion (LPBF), Prog. Addit. Manuf. (2025), https://doi.org/10.1007/s40964-025-01029-0.

[10] C. Brown, M. Brochu, M.A. Shandiz, A. Kumar, Powder bed fusion methods and related apparatus WO2022123224A1, (2022).

[11] S.E. Atabay, P. Wanjara, F. Bernier, S. Sarafan, J. Gholipour, J. Soost, R. Amos, P. Patnaik, M. Brochu, In envelope additive/subtractive manufacturing and thermal post-processing of Inconel 718, Materials 16 (2023), https://doi.org/10.3390/ma16010001.

[12] ISO, ISO 16610-62:2023, Int. Organ. Stand. Switz, . (2023).

[13] J.M. Oblak, D.F. Paulonis, D.S. Duvall, Coherency strengthening in Ni base alloys hardened by DO22 γ' precipitates, Metall. Trans. 5 (1974) 143–153, https://doi.org/10.1007/BF02642938.

[14] D. Mukherji, R. Gilles, B. Barbier, D. Del Genovese, B. Hasse, P. Strunz, T. Wroblewski, H. Fuess, J. Rösler, Lattice misfit measurement in Inconel 706 containing coherent γ' and γ'' precipitates, Scr. Mater. 48 (2003) 333–339, https://doi.org/10.1016/S1359-6462(02)00456-6.

[15] A. Sarkar, P. Mukherjee, P. Barat, T. Jayakumar, S. Mahadevan, S.K. Rai, Lattice misfit measurement in inconel 625 by X-ray diffraction technique, Int. J. Mod. Phys. B 22 (2008) 3977–3985, https://doi.org/10.1142/S0217979208048772.

[16] S. Zhang, X. Lin, L. Wang, X. Yu, Y. Hu, H. Yang, L. Lei, W. Huang, Strengthening mechanisms in selective laser-melted Inconel718 superalloy, Mater. Sci. Eng. A 812 (2021) 141145, https://doi.org/10.1016/j.msea.2021.141145.

[17] J.E. Campbell, R.P. Thompson, J. Dean, T.W. Clyne, Comparison between stress-strain plots obtained from indentation plastometry, based on residual indent profiles, and from uniaxial testing, Acta Mater. 168 (2019) 87–99, https://doi.org/10.1016/j.actamat.2019.02.006.

[18] S. Ooi, R. Reiff-Musgrove, M. Gaiser-Porter, M. Steinbacher, I. Griffin, J. Campbell, M. Burley, M. Warwick, H. Vaka, C. Fang, T.W. Clyne, Profilometry-based indentation plastometry testing for characterization of case-hardened steels, Adv. Eng. Mater. 25 (2023), https://doi.org/10.1002/adem.202201512.

[19] D. Wang, Y. Yang, Z. Yi, X. Su, Research on the fabricating quality optimization of the overhanging surface in SLM process, Int. J. Adv. Manuf. Technol. 65 (2013) 1471–1484, https://doi.org/10.1007/s00170-012-4271-4.

[20] R.J. Lancaster, N.C. Barnard, B. Haigh, E.E. Sackett, P.E. May, R.J. Douglas, D. Britton, S.P. Jeffs, Evaluating the efficacy of alternative small scale test methodologies in deriving the mechanical properties of additive manufactured materials, J. Mater. Res. Technol. 26 (2023) 9328–9345, https://doi.org/10.1016/j.jmrt.2023.09.224.

[21] A.A.H. Ameri, N.N. Elewa, M. Ashraf, J.P. Escobedo-Diaz, General methodology to estimate the dislocation density from microhardness measurements, Mater. Charact. 131 (2017) 324–330, https://doi.org/10.1016/j.matchar.2017.06.031.

[22] C.L. Li, Q.S. Mei, J.Y. Li, F. Chen, Y. Ma, X.M. Mei, Hall-Petch relations and strengthening of Al-ZnO composites in view of grain size relative to interparticle spacing, Scr. Mater. 153 (2018) 27–30, https://doi.org/10.1016/j.scriptamat.2018.04.042.

[23] X. Zhou, Z. Feng, L. Zhu, J. Xu, L. Miyagi, H. Dong, H. Sheng, Y. Wang, Q. Li, Y. Ma, H. Zhang, J. Yan, N. Tamura, M. Kunz, K. Lutker, T. Huang, D.A. Hughes, X. Huang, B. Chen, High-pressure strengthening in ultrafine-grained metals, Nature 579 (2020) 67–72, https://doi.org/10.1038/s41586-020-2036-z.

[24] S. Sui, H. Tan, J. Chen, C. Zhong, Z. Li, W. Fan, A. Gasser, W. Huang, The influence of laves phases on the room temperature tensile properties of Inconel 718 fabricated by powder feeding laser additive manufacturing, Acta Mater. 164 (2019) 413–427, https://doi.org/10.1016/j.actamat.2018.10.032.

[25] G. Lehmann, On solid solution hardening of metal crystals, J. Phys. D. Appl. Phys. 2 (1969) 126–128, https://doi.org/10.1088/0022-3727/2/1/419.

[26] H.A. Roth, C.L. Davis, R.C. Thomson, Modeling solid solution strengthening in nickel alloys, Metall. Mater. Trans. A Phys. Metall. Mater. Sci. 28 (1997) 1329–1335, https://doi.org/10.1007/s11661-997-0268-2.

[27] H.L. Wei, J. Mazumder, T. DebRoy, Evolution of solidification texture during additive manufacturing, Sci. Rep. 5 (2015), https://doi.org/10.1038/srep16446.

[28] D.E. Jodi, T. Kitashima, Y. Koizumi, T. Nakano, M. Watanabe, Manufacturing single crystals of pure nickel via selective laser melting with a flat-top laser beam, Addit. Manuf. Lett. 3 (2022) 100066, https://doi.org/10.1016/j.addlet.2022.100066.

[29] A. Kumar, M.A. Shandiz, M. Brochu, Solution heat treatment of support-free IN625 overhang sections fabricated via laser powder bed fusion (LPBF), Prog. Addit. Manuf. 10 (2025) 7085–7099, https://doi.org/10.1007/s40964-025-01029-0.M.B.

[30] Y. Hu, X. Lin, Y. Li, Y. Ou, X. Gao, Q. Zhang, W. Li, W. Huang, Microstructural evolution and anisotropic mechanical properties of Inconel 625 superalloy fabricated by directed energy deposition, J. Alloys Compd. 870 (2021) 159426, https://doi.org/10.1016/j.jallcom.2021.159426.

[31] K. Gruber, R. Dziedzic, B. Kuźnicka, B. Madejski, M. Malicki, Impact of high temperature stress relieving on final properties of Inconel 718 processed by laser powder bed fusion, Mater. Sci. Eng. A 813 (2021), https://doi.org/10.1016/j.msea.2021.141111.

[32] T.R. Smith, J.D. Sugar, C. San Marchi, J.M. Schoenung, Strengthening mechanisms in directed energy deposited austenitic stainless steel, Acta Mater. 164 (2019) 728–740, https://doi.org/10.1016/j.actamat.2018.11.021.

[33] S. Ghosh, L. Ma, N. Ofori-Opoku, J.E. Guyer, On the primary spacing and microsegregation of cellular dendrites in laser deposited Ni-Nb alloys, Model. Simul. Mater. Sci. Eng. 25 (2017) 1–25, https://doi.org/10.1088/1361-651X/aa7369.

[34] J. Jang, D. Van, S.H. Lee, Precipitation kinetics of secondary phases induced by heat accumulation in the deposit of Inconel 718, Addit. Manuf. 55 (2022) 102831, https://doi.org/10.1016/j.addma.2022.102831.

[35] R.Y. Zhang, H.L. Qin, Z.N. Bi, J. Li, S. Paul, T.L. Lee, S.Y. Zhang, J. Zhang, H. B. Dong, Evolution of lattice spacing of gamma double prime precipitates during aging of polycrystalline Ni-base superalloys: an In situ investigation, Metall. Mater. Trans. A Phys. Metall. Mater. Sci. 51 (2020) 574–585, https://doi.org/10.1007/s11661-019-05536-y.

[36] X. Wang, L.N. Carter, B. Pang, M.M. Attallah, M.H. Loretto, Microstructure and yield strength of SLM-fabricated CM247LC Ni-Superalloy, Acta Mater. 128 (2017) 87–95, https://doi.org/10.1016/j.actamat.2017.02.007.

[37] S. Ghaemifar, H. Mirzadeh, Precipitation kinetics of gamma double prime phase during direct aging treatment of Inconel 718 superalloy additively manufactured by selective laser melting, J. Mater. Res. Technol. 27 (2023) 4248–4255, https://doi.org/10.1016/j.jmrt.2023.10.267.

[38] W. Li, J. Ma, H. Kou, J. Shao, X. Zhang, Y. Deng, Y. Tao, D. Fang, Modeling the effect of temperature on the yield strength of precipitation strengthening Ni-base superalloys, Int. J. Plast. 116 (2019) 143–158, https://doi.org/10.1016/j.ijplas.2019.01.002.